Int. J. Electrochem. Sci., 14 **(2019)** 1713 – 1724, doi: 10.20964/2019.02.76

International Journal of
ELECTROCHEMICAL
SCIENCE
www.electrochemsci.org

Image Analysis of Synthesized Corrosion Products Applied to In-situ Analysis of Q235 Steel under Simulated Marine Atmosphere

Xinxin Zhang[1], Zhiming Gao[1,], Yan Xiu[2], Wenbin Hu[1], Zhipeng Wu[1], Lihua Lu[1], Lianheng Han[1]*

[1] Tianjin Key Laboratory of Composite and Functional Materials, School of Material Science and Engineering, Tianjin University, Tianjin 300350, P. R. China
[2] Faculty of science, Tianjin Chengjian University, Tianjin 300384, P. R. China
[*]E-mail:gaozhiming@tju.edu.cn

Received: 2 November 2018 / *Accepted:* 18 December 2018 / *Published:* 5 January 2019

The main constituents of rust layers of carbon steel generated in marine atmosphere, goethite and lepidocrocite, have been synthesized in the laboratory. The images of synthesized corrosion products with different mixing ratios were obtained using the established image acquisition system. To get the characteristic information, images were analyzed based on colorimetry theory. Finally, an artificial neural network was employed to determine a relationship between the mixing ratios and achieved image characteristics. Mass fraction of goethite, protective constitute of rust layers, could be obtained based on image analysis of rust layers. The corrosion behavior of Q235 steel under the simulated marine atmosphere was investigated by above method. And the result showed a good correlation with electrochemical information.

Keywords: rust layers; goethite; image analysis; artificial neural network

1. INTRODUCTION

Atmospheric corrosion is the most common form of metal corrosion for a mass of metal exposed in atmosphere. Modern industry has higher requirement about corrosion resistance of metal which demands further study in atmospheric corrosion mechanism. As is well-known, how to realize in-situ analysis of corroded metals is difficult and many researchers have been making unremitting efforts [1-4]. For example, Toshiaki [1] used in situ Raman spectroscopy to monitoring the development of rust layers on weathering steel. And in the earlier works by Pan et al. [2], electrochemical methods combined with morphology analysis methods were used to investigate atmospheric corrosion behavior of printed circuit boards. Various works have been tried, and among them it is rare using images of rust layers to

realize in-situ analysis.

In fact, amounts of information about corrosion behaviors of metals could be got based on image analysis [5-11], such as corrosion classification [5-6], corrosion extent [7-9], corrosion form [10] and so on. In this work, goethite and lepidocrocite have been synthesized in the lab. Images of those synthesized corrosion products obtained to analysis the constituents of rust layers on carbon steel under atmospheric atmosphere. Juan et al. [12] found goethite and lepidocrocite were the main constituents of short-term steel corrosion products formed in tropical marine environment. According to the research of Antony [13], rust layer is constituted mainly by stable goethite (α-FeOOH) and electrochemically active lepidocrocite (γ- FeOOH), in addition he proposed α/γ as the protective ability index. Hence it would be significant to confirm the ratio of goethite to lepidocrocite of rust layers [14]. The artificial neural network (ANN) built in this paper was just to realize the purpose that get to know the ratio of goethite and lepidocrocite through image processing [15].

Traditional image analysis methods transfer images to grayscale images before further process which lost lots of information especially for rust layers be rich of color [5, 16]. According to colorimetry theory which was proposed by Young in 1802, the color image of rust layers is composed of numerous pixels, and each pixel is associated with three digits of red, green, and blue (RGB) varying from 0 to 255 with 8 bit [17]. The RGB color space converts color image to a three-dimensional matric making data more analyzable. In-situ analysis of atmospheric corrosion could be realized through statically analysis to the matric in this work. At the same time, electrochemical information obtained from wire beam electrode test was analyzed combined with image analysis of rust layers of Q235 steel.

2. EXPERIMENTAL AND IMAGE ANALYSIS

2.1 Synthesis and characterization

Goethite and lepidocrocite were obtained by direct precipitation [18-20]. Goethite was synthesized by pouring 100ml freshly prepared Fe $(NO_3)_3 \cdot 9H_2O$ into a 2l polyethylene flask and adding 155ml 5MNaOH solution rapidly under stirring. This mixture was immediately diluted to 2l as red-brown precipitate generated and then stored at 60°C for 60h.Lepidocrocite was synthesized by dissolving 11.93g $FeCl \cdot 4H_2O$ in 150ml distilled water and adjusting the PH of the solution to 6.8 by adding 5MNaOH solution. Blow air with the pump at the flow rate of 100ml/min. After about 2h, the completion of the oxidation reaction was obtained, as revealed by the orange color of the suspension.

The characterization of the samples was extracted by the following conventional means. X-ray diffraction (XRD) patterns of the synthetic compounds were measured by a PANalytical diffractometer (D/max 40 kV) with CuKα radiation. Morphologies were observed using a scanning electron microscopy (SEM). Image of synthesized powders and rust layers of Q235 steel were obtained using VHX-2000 digital microscope under fixed condition to get repeatable and comparable data [21-22].

2.2 Wire beam electrode (WBE) test

Wire beam electrode was made of 100 fine Q235 steels electrode sealed with epoxy resin. During the test, the surface of the electrode kept upwards and covered with lens paper, 3μm in thickness. 0.01mol/L NaCl solution wetted lens papers and keep 2-3 mm lower than the electrode surface to simulate marine atmosphere, showed in Figure 1 [23]. CST520 was used to collect potential and current of every Q235 electrode relative to saturated calomel electrode.

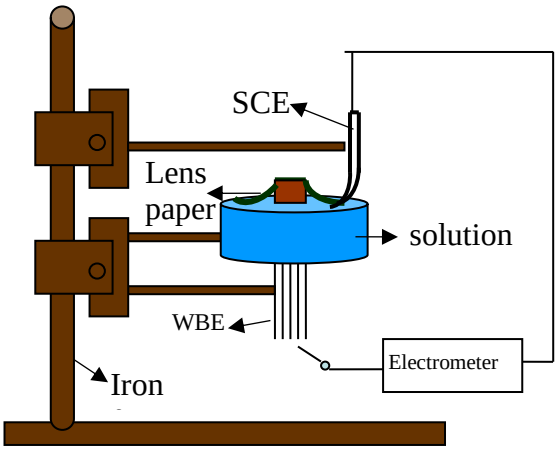

Figure 1. Schematic diagram of WBE experimental measurement

2.3 Image processing method

Most digital image processing techniques are for black and white or grayscale images. However, metallic corrosion topography images are rich in color and color images can provide more information than grayscale images. To realize quantitative analysis of the color information of images, a mathematical model has been established. According to colorimetry theory, any color can be obtained by mixing three primary colors in a certain proportion, that is,

$C = aC_1 + bC_2 + cC_3$

Where C1, C2, C3 are the three primary colors. And a, b, c are weights correspondingly.

Goethite synthesized in the lab presents yellow the same as reported by Fu [18], as shown in Figure 2. With program in Matlab, RGB values of all pixels in this image were statistically analyzed. Distribution of RGB values are shown in figure 3. According to waveform characteristics, frequencies at values of R component were 110, 130, 150, 170, 190, values of G component were 90, 110, 130, 150, 170, and values of B component were10, 25, 40, 55, 70, were selected as image characteristics (described as F). Chosen values range cover the corresponding RGB distribution area, which can reflect the distribution characteristics of each brightness values.

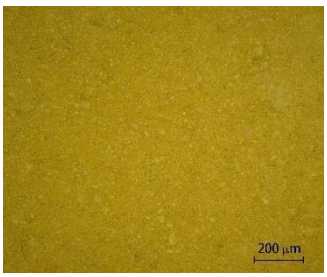

Figure 2. Image of goethite synthesized in Tianjin Key Laboratory of Composite and Functional Materials

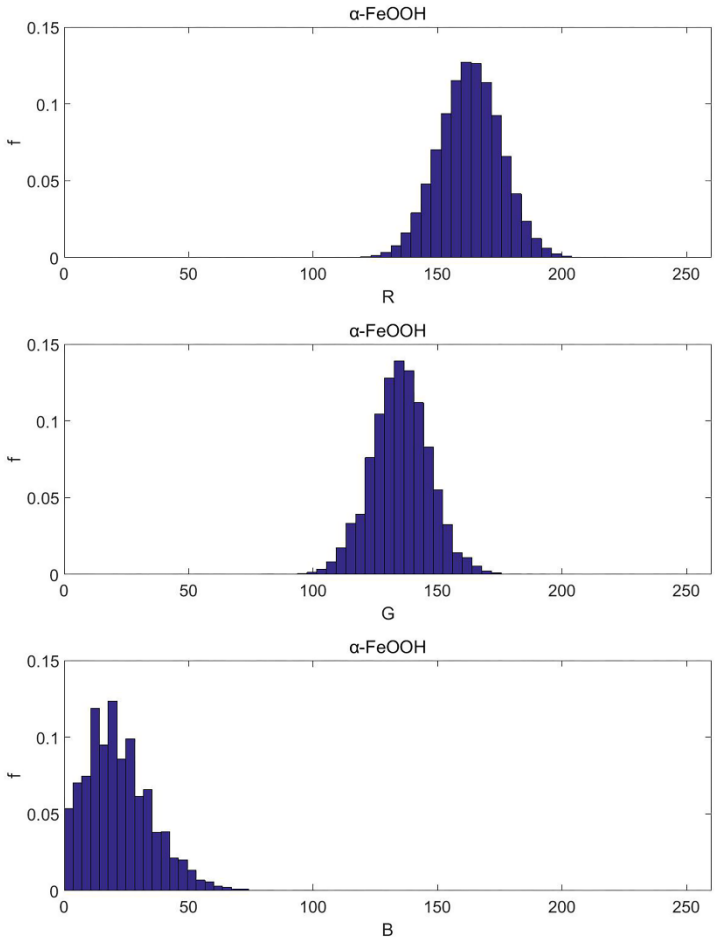

Figure 3. Histogram of RGB distribution of goethite

3. RESULTS AND DISCUSSION

3.1 Characterization of synthesized samples

The XRD patterns of the synthesized powders are shown in Figure 4 and Figure 5. Based on comparison with JCPDS card (29-0713), the first sample shown in Figure 1 contains six distinct peaks corresponding to the (020), (110), (120), (130), (111), (221) and (151) planes of α-FeOOH. In the XRD

patterns of Figure 1 (b), the sample has distinct peaks correspond to the (020), (120), (091), (111), (220), (151), (231) and (171) planes of γ-FeOOH (JCPDS card #74-1877) [21,22].

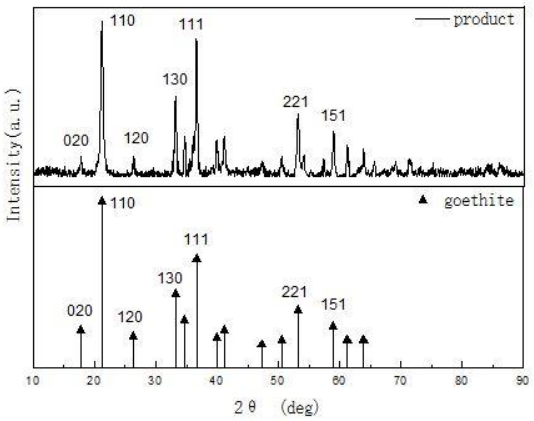

Figure 4.XRD patterns of goethite compared with standard JCPDS cards, D/max 40 kV

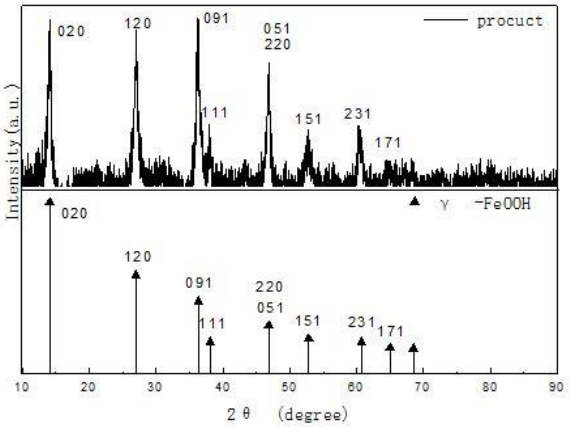

Figure 5.XRD patterns of lepidocrocite compared with standard JCPDS cards, D/max 40 kV

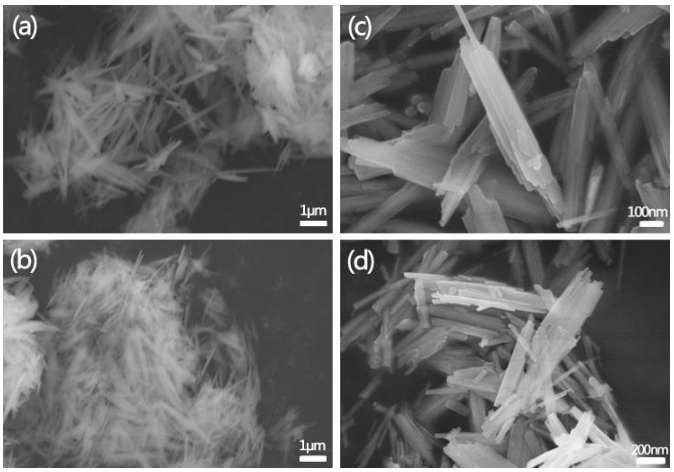

Figure 6. SEM images of the synthesized powders: α-FeOOH (a), (b); γ-FeOOH (c), (d)

The synthesized α-FeOOH powders are typically needle-like with single crystals measuring between 1.5 and 2.0 μm in length, as shown in Figure 6 (a) and (b) [18]. The crystals of γ-FeOOH are lath-like and ~500 nm in length, as shown in Figure 6 (c) and (d) [22, 24].Both of them appear to be well crystallized.

3.2Constituent analysis based on the artificial neural network

Images of the synthesized powders were obtained using a VHX-2000 digital microscope. The goethite phase (α-FeOOH) appears as yellow, while lepidocrocite (γ-FeOOH) appears orange-red as shown in Figure 2 and Figure 7.

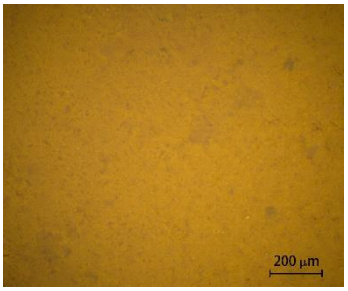

Figure 7. Image of lepidocrocite synthesized in Tianjin Key Laboratory of Composite and Functional Materials

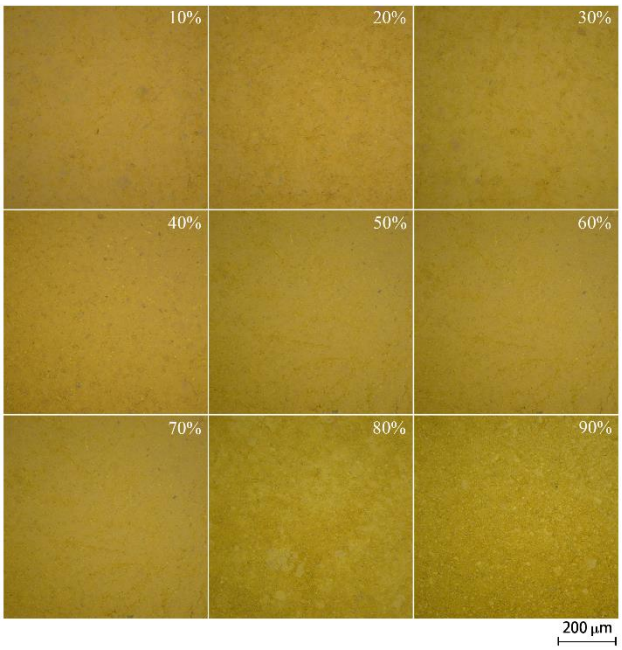

Figure 8. Images of goethite – lepidocrocite system with the goethite mass fraction changed from 10% to 90%

To determine the mass fraction of goethite in the goethite - lepidocrocite system, the synthesized

goethite and lepidocrocite powders were mixed with the goethite mass fractions of 10, 20, 30, 40, 50, 60, 70, 80, and 90%, as shown in Figure 8. Based on the above method, the RGB values of all pixels in these images were statistically analyzed. The distributions of RGB frequency are shown in Figure 9. Fifteen characteristic frequencies from each image were selected as shown in table 1.

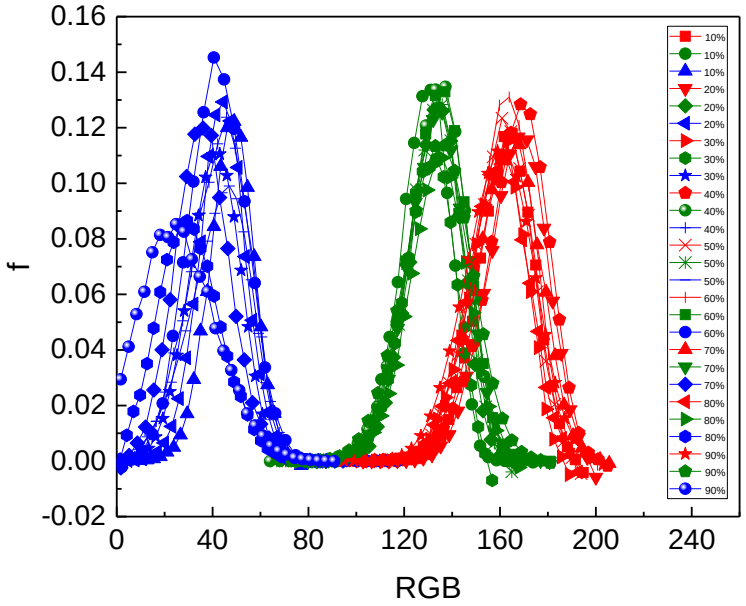

Figure 9. Distribution of RGB values with mass fraction of goethite changed from 10% to 90%

Afterwards, the ANN was used to determine a relationship between the image characteristics and the goethite mass fraction. The net comprised three parts: an input layer containing 15 neurons related to the fifteen image characteristic frequencies, hidden layers, and an output layer representing the goethite mass fraction, as shown in Figure 10.

Table 1. Relation of the ratio of α-FeOOH (wt%) and RGB characters of samples ($F \times 10^3$)

10	20	30	40	50	60	70	80	90
0	0	0	0	0	0	0	0	0.2
2.3	1.2	5.9	2.3	7	5.2	3	6.2	1.7
61	43.8	70.1	38.2	57.9	84.3	47.8	86.4	91.7
84.8	140.3	110.7	145.6	78.4	98.8	120.2	104.5	100.6
0.1	8.9	0	10.7	0.5	2.2	5.9	1.4	1.6
0.1	0.7	0.1	0.5	0	0	0	0	0.3
24.8	6.8	16.7	16	20.8	11.7	12	17.5	23.3
136.5	105.8	122.6	121.3	130.7	120.2	121.5	99.7	110.3
1.2	29.6	4.1	40.7	23.6	50.6	40.5	43.9	65
0	0	0	0.2	0	0.1	0.8	0	1.6
0.2	0.5	1.3	2.7	4.1	1	3.8	24.8	46.4
4.2	16.7	34.5	28.7	36	29.2	76.1	89.9	47.7
95.6	128.6	119.1	112	90.6	158	143.6	61.7	46.3
106.7	71.3	44.8	56.4	67.8	83	21.4	15.5	16.6
0.5	1.7	0.2	1.2	1.1	2.2	1.8	1.1	1.6

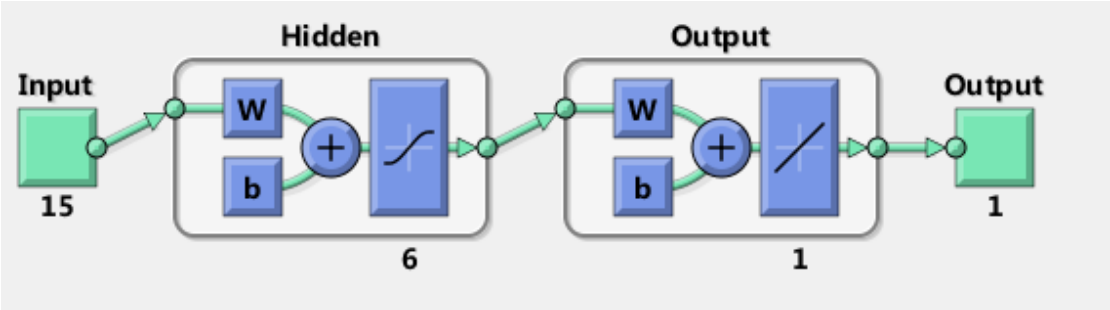

Figure 10. Structure of the artificial neural network

After training, the relationship between image characteristics and the goethite mass fraction was set and the mathematical mapping was stored in the training net. The results in Figure 11 show that the correlation coefficient of the network and target output reach 0.99721, indicating successful training.

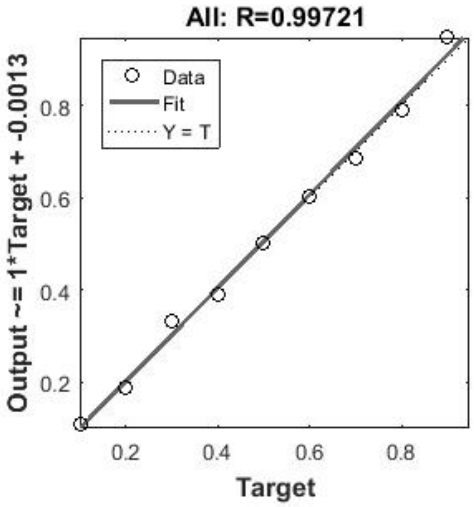

Figure 11. Fitting analysis chart of the neural network

3.3 Image characteristics and electrochemical information of Q235 steel

The potentials and currents of one hundred fine Q235 steel electrodes were recorded during the wire beam electrode (WBE) test. Previous work, reported that the corrosion of Q235 steel under a simulated marine atmosphere was initiated around pearlite phases and presented characteristics of local corrosion [25]. Through statistical analysis of the potentials recorded during the test, the changing trends of the average corrosion potential and the corrosion potential standard deviation were obtained as shown in Figure 12, and 13. The decrease of the corrosion potential standard deviation indicates a decrease in the corrosion inhomogeneity of the Q235 steel.

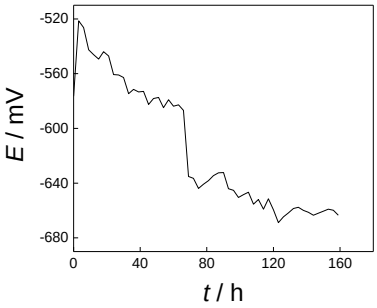

Figure 12. Mean corrosion potentials varying with time

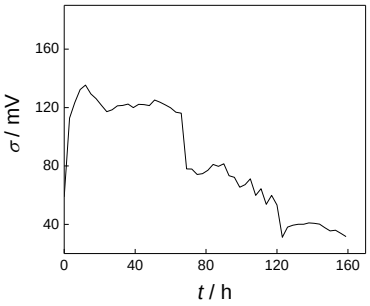

Figure 13. Corrosion potential standard deviation varying with time

Figure 14 shows corroded layers of the Q235 steel from the inner layer (d) to the outer layer (a) after six days of simulated marine atmospheric corrosion testing. The method of analyzing atmospheric corrosion using image characteristics was applied to these rust layers. In the previous work [25], three peaks of the RGB distribution diagram were selected as the image characteristics. In this work, fifteen characteristics were abstracted to better describe the image and obtain more representative data.

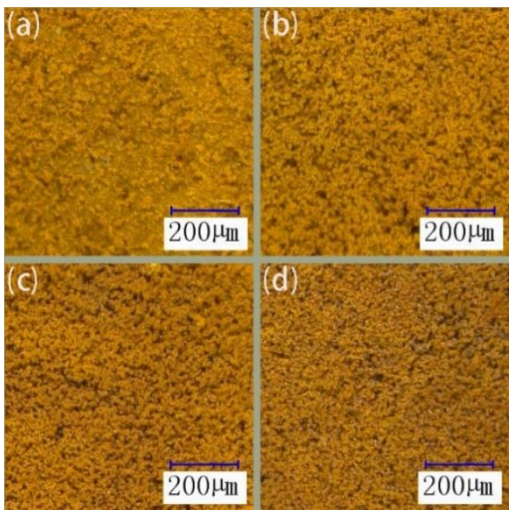

Figure 14. Images of rust layers from outer to inner (a)~(d) 0.3-0.5 mm in depth

The characteristics obtained by image analysis are shown in Table 2.

Table 2. Image characters of rust layers ($F \times 10^3$)

(a)	(b)	(c)	(d)
1.6	9.9	8.5	10.5
11.9	24.5	39.8	57.4
59.7	55.7	68.6	89.7
85.5	92.3	96.5	85.8
53.9	95.9	71.1	50.9
11.8	80.3	64.4	77.2
43.8	92.8	96.2	96.2
76.2	74.7	73.5	59.3
18.6	30.4	13.4	15.5
2	0.9	1.3	1.6
90.8	91.1	99	91.3
25.7	27.7	63.9	115.7
2.9	5.7	27.7	64.3
0.3	0.7	10.9	26.7
0	0	1.8	7.6

Using the fifteen characteristics of each image as the input for the ANN built above, the net output of the goethite mass fraction would be obtained.

Table 3. Analysis results

Rust layers (Figure 6)	Out-put（α-FeOOH wt%）
(a)	0.6935
(b)	0.6527
(c)	0.3824
(d)	0.2827

The process of removing the lens paper removed the outmost rust layers, leaving the internal layers. In Table 2, the ratio of goethite to lepidocrocite in the rust layer nearest the substrate is lower than that in the outer layer. It can be inferred that lepidocrocite is generated on the metal matrix early in corrosion. As time increases, the proportion of goethite is increased. It has been reported that lepidocrocite is transformed into other corrosion products, which is probably the reason for the change in the proportions of goethite and lepidocrocite in the rust layers of the Q235 steel [26-30]. Goethite is supposed to be a protective constituent [13] that is not transformed to other kinds of products because it has a low free energy.

As shown in the electrochemical information in Figure 13, the standard deviation of the corrosion potential of the Q235 steel electrodes is gradually decreased with increasing corrosion time. The

characteristics of uniform corrosion appear. It is concluded that the corrosion mode of Q235 steel under a simulated marine atmosphere is changed from localized to uniform. Through the analysis of the rust layers, the increase of the goethite composition enhanced the resistance of the rust layers and blocked oxygen diffusion, thus contributing to the trend observed during the WBE test.

4. CONCLUSIONS

In this study, goethite and lepidocrocite were synthesized in the laboratory. The image characteristics of the synthesized powders with different mixing ratios were abstracted based on colorimetry theory. After training of the ANN, the relationship between image characteristics and the goethite mass fraction was stored. The result showed the correlation coefficient of the network output and the target output reaching 0.99721, indicating successful training.

In the WBE test, the average and standard deviation of the corrosion potential of Q235 electrodes was decreased with increasing corrosion time. The electrochemical information obtained during the test showed a decreasing trend in the corrosion inhomogeneity of Q235 steel.

According to the image analysis of rust layers generated during the WBE test, the protective constituent of rust layers, goethite, was increased with increasing corrosion time, which contributed to the transformation of the corrosion mode of Q235 steel from localized to uniform corrosion. The image analysis of the rust layers presented good correlation with the obtained electrochemical information.

ACKNOWLEDGEMENTS
This project is supported financially by National Natural Science Foundation of China (No. 51671144, No. 51131007, No. 51871164) and Supporting Plan Project of Tianjin City (16YFZCGX00100) and Natural Science Foundation of Tianjin (No. 17JCTPJC47100)

References

1. O. Toshiaki and T. Shozo, *J. Solid State Electrochem.*, 19 (2015) 3559.
2. P. Yi, K. Xiao and K. K. Ding, *Chin J Nonferrous Met*, 26 (2016) 1146.
3. X. N. Liao, F. H. Cao, A. N. Chen, W. J. Liu, J. Q. Zhang and C. N. Cao, *Chin J Nonferrous Met*, 22 (2012) 1239.
4. Y. Xie, Y. Wang and Y. Men, *Int. J. Electrochem. Sci.*, 7 (2012) 10679.
5. R. M. Pidaparti, B. S. Aghazadeh, A. Whitfield, A. S. Rao and G. P. Mercier, *Corros. Sci.*, 52 (2010) 3661.
6. K. Y. Choi and S. S. Kim, *Corros. Sci.*, 47 (2005) 1.
7. D. H. Xia, C. Ma, S. Z. Song, W. X. Jin, Y. Behnamian, H. Q. Fan, J. H. Wang, Z. M. Gao and W. B. Hu, *Corros. Sci.*, 120 (2017) 251.
8. O. E. Garcia and F. Corvo, *Electrochem. Commun.*, 12 (2010) 826.
9. Z. M. Gao, X. B. Han, L. H. Dang, Y. Wang and H. C. Bi, *Int. J. Electrochem. Sci.*, 7 (2012) 9202.
10. P. Platt, D. Lunt, E. Polatidis, M. R. Wenman and M. Preuss, *Corros. Sci.*, 111 (2016) 344.
11. J. M. Salgado, J. U. Chavarin and D. M. Cruz, *Int. J. Electrochem. Sci.*, 7 (2012) 1107.
12. J. A. Jaen, J. Iglesias and C. Hernandez, *Int. J. Corros.*, 2012 (2012) 11.
13. H. Antony, L. Legrand, L. Marechal, S. Perrin, P. Dillmann and A. Chausse, *Electrochim. Acta*, 51

(2005) 745.
14. P. Qiu, Z. S. Chen, H. F. Yang, L. J. Yang, L. Luo and C. F. Chen, *Int. J. Electrochem. Sci.*, 11 (2016) 10498.
15. R. Vera and S. Ossandon, *Int. J. Electrochem. Sci.*, 9 (2014) 7131.
16. B. N. Nelson, P. Slebodnick, E. J. Lemiuex, W. Singleton, M. Krupa, K. Lucas, D. Thomas and A. Seelinger, Wavelet applications VIII, 8th Annual Conference on Wavelet Applications, Orlando, USA, 2001, 134.
17. W. Li, R. Q. Zhang, H. T. Wang, W. Jiang, L. Wang, H. Li, T. Wu and Y. P. Du, *Anal. Methods.*, 8 (2016) 2887.
18. H. B. Fu and X. Quan, *Chemosphere*, 63 (2006) 403.
19. H. Antony, S. Peulon, L. Lergrand and K. Chausse, *Electrochim. Acta*, 50 (2004) 1015.
20. M. Sheydaei and S. Aber, *CLEAN-Soil Air Water*, 41 (2013) 890.
21. T. Ishikawa, W. Sakata, A. Yasukawa and K. Kandori, *Colloids Surf.*, 136 (1998) 183.
22. W. Han, C. Pan, Z. Y. Wang and G. C. Yu,*J. Mater. Eng. Perform.*, 24 (2015) 864.
23. S. X. Wang, D. X. Liu, N. Du, Q. Zhao and J. H. Xiao, *Int. J. Electrochem. Sci.*, 11 (2016) 2534.
24. Q. X. Li, Z. Y. Wang, W. Han and E. H. Han,*Corros. Sci.*, 50 (2008) 365.
25. X. X. Zhang, Z. M. Gao, W. B. Hu, Z. P. Wu, L. H. Han, L. H. Lu, Y, Xiu and D. H. Xia, *J. Chin. Soc. Corros. Prot.*, 37 (2017) 444.
26. Y. Y. Chen, H. J. Tzeng, L. I. Wei and H. C. Shih, *Corros. Sci.*, 47 (2005) 1001.
27. Y. L. Zhou, X. J. Zhang, T. Jia and Z. Y. Liu, *J. Iron Steel Res. Int.*, 22 (2015) 496.
28. Z.Q. Wang, J.Q. Wang, Y. Behnamian, Z. Gao, J. Wang, D.H. Xia, *Corros. Sci. Eng. Technol*., 53 (2018) 206.
29. D.H. Xia, C. Ma, S. Song, L. Ma, J. Wang, Z. Gao, C. Zhong, W. Hu. *Sens. Actuators, B*, 252 (2017) 353
30. D.H. Xia, J. Wang, Z. Wu, Z. Qin, L. Xu, W. Hu, Y. Behnamian, J.L. Luo, *Sens. Actuators, B*, 280 (2019) 235.